HHS Public Access

Author manuscript

*Nanoscale*. Author manuscript; available in PMC 2018 September 26.

Published in final edited form as:

*Nanoscale*. 2018 August 07; 10(29): 13857–13866. doi:10.1039/c8nr04255a.

# The aerolysin nanopore: from peptidomic to genomic applications

**Yong Wang**[a], **Li-Qun Gu**[b], and **Kai Tian**[b]

[a]Virginia G. Piper Biodesign Center for Personalized Diagnostics, The Biodesign Institute, Arizona State University, Tempe, AZ 85287, USA. ywan1012@asu.edu

[b]Department of Bioengineering and Dalton Cardiovascular Research Center, University of Missouri, Columbia, MO 65211, USA. gul@missouri.edu

## Abstract

The aerolysin pore (ARP) is a newly emerging nanopore that has been extensively used for peptide and protein sensing. Recently, several groups have explored the application of ARP in detecting genetic and epigenetic markers. This brief review summarizes the current applications of ARP, progressing from peptidomic to genomic detection; the recently reported site-directed mutagenesis of ARP; and new genomic DNA sensing approaches, and their advantages and disadvantages. This review will also discuss the perspectives and future applications of ARP for nucleic acid sequencing and biomolecule sensing.

## 1. Introduction

Aerolysin is a pore-forming cytolytic bacterial toxin. Its activation[1] and nucleotide sequence[2] were first analyzed in the 1980s by Dr Howard and coworkers. Aerolysin is now emerging as a new nanopore system, with distinct differences from the widely used alpha-hemolysin nanopore system. ARP was first used for α-helical peptide translocation studies in 2006[3] and has since been used intensively for peptide and protein sensing, including small protein analysis,[4] to study protein unfolding dynamics,[5] to distinguish unfolded protein states,[6] for polysaccharide detection,[7] to analyze enzymatic degradation of long polysaccharide chains,[8] to detect botulinum toxin,[9] to analyze protein unfolding and translocations,[10] to detect low molecular weight (140 Da) poly(ethylene glycol) (PEG) at the single-molecule level,[11] for high-resolution size discrimination of PEG molecules,[12] to evaluate the physical parameters governing an unfolded protein translocation,[13] to identify single oligo-nucleotide photoisomers,[14] and for ultrasensitive detection of cancer cells by enzymatic amplification.[15] Most recently, Drs Pelta and Oukhaled's group has reported that ARP can be used to identify amino acids in short peptides, detecting and characterizing a few dozen impurities in a high-purity (>98%) commercial peptide sample. This study demonstrated the possible utility of ARP in the field of single-molecule proteomics.[16]

Correspondence to: Yong Wang; Li-Qun Gu.

Conflicts of interest

The authors declare no competing financial interest.

Subsequently, a report from Dr Long's group demonstrated that both the charge and length of a peptide affect its translocation through ARP.[17]

As discussed above, significant effort has focused on peptidomic applications using ARP, but very few studies have ana lyzed its utility in nucleic acid detection. Pastoriza-Gallego *et al.* (2014)[10] and Payet *et al.* (2015)[18] found that ARP had extremely low capture rates for 3 μM of single-stranded DNAs (50–60 nucleotides). They found that ARP cannot capture DNA below 100 mV, and that DNA translocation rates were about 10-fold lower than with the widely used alpha-hemolysin pore. This significantly limits the utility of the ARP for nucleic acid detection. However, several recently reported studies indicate the possibilities of ARP for sensing of DNAs. This mini review will focus on studies using ARP for genomic applications.

## 2. ARP structure

Aerolysin is a member of a major class of β-pore-forming toxins (β-PFTs). ARP is a heptameric pore-forming toxin and it can be spontaneously inserted into lipid bilayers to form a nanoscale pore. So besides their role in osmotic lysis and cell death during microbial infection, ARP has also been used as nano-sensors with lots of applications in biomolecule detection and identifications. Studies have combined X-ray crystallography, cryo-electron microscopy and computational modeling data to determine the conformational intermediates, aerolysin mutants in their monomeric and heptameric forms, as well as the structure of the ARP in an atomic model (Fig. 1a and b).[19,20] Molecular dynamics simulations on a $10^2$ ns timescale were stable for both wild-type and Y221G mutant pro-aeroly-sins. After refinement using a molecular dynamics flexible fitting procedure, the best heptameric model had a cross-correlation coefficient with the cryo-EM map of 0.79. Experiments observed that steering out the pre-stem loop in molecular dynamics leads to a remarkable rearrangement of domain 4 with respect to domain 3. The aerolysin prepore goes through several conformational changes like initial rearrangements, oligomerization, the concentric barrel fold, tightly bound together by hydrophobic interactions, and then forms the final ARP with a β-barrel length of ~87 Å and a diameter of ~8.75 Å (average distance between the opposite strand backbone).[19] Structurally, the ARP has multiple charged residues in its channel wall, particularly around both openings to the pore. Negatively charged residues include E237, E252, E254, and E258 near the *trans* ARP entrance, and D209, D216 near the *cis* entrance, while positive charges contributed by K238, K242, K244, and K246 localize towards the *trans* barrel, while charges from R220, R282, and R288 cluster around the *cis* entrance. These studies suggested an ultrastability of ARP and its stoichiometry.[19,20] Compared to other reported biological nano-pores, ARP exhibits the advantage of stability over a broad pH range.[21,22]

## 3. Direct discrimination of A, T, C and G nucleobases, as well as methylcytosine (mC) from cytosine in an oligonucleotide in the ARP

Similar to previous reports, Long's group in 2016[21] (see the detailed protocol of 2017[23]) determined that ARP could not capture long, single-stranded DNA molecules, but this conductance variation could discriminate the length of high-concentrations (1 μM) of short

(2–10 nt) poly(dA) oligonucleotides at a single nucleotide resolution (Fig. 2a) under a wide range of pH conditions where the ARP remained stable. They also demonstrated that ARP could distinguish individual oligonucleotide lengths and monitor the stepwise cleavage of these oligonucleotides by exonuclease I in real time (Fig. 2b), revealing a possible application of ARP in genetic studies. However, only polydeoxyadenines were used in this study and it is not clear if similar results can be obtained with dC, dT or dG polynucleotides or bases. Using the total internal reflection fluorescence (TIRF) experiment (Fig. 2c), Long's group identified that a 5′-AA-3′ dinucleotide with a 3′−6-carboxyfluorescein fluorophore tag[21] and a 5′-ACTG-3′ tetranucleotide with a 5′-hexachloro-fluorescein tag[24] can translocate from *cis* to *trans* through the ARP. Conversely, the 5′-ACTG-3′ tetranucleotide does not produce any current signals during *cis* or *trans* translocation through alpha-hemolysin, the most widely used nanopore system. This difference may be due to the different charge distribution and smaller size of the ARP.[24] These results suggest that ARPs may be more suitable for studies of short nucleic acids, as it exhibits high sensitivity and prolonged translocation for the molecules to enhance their detection and discrimination.

In a follow-up study, Long's group studied the ARP trans-location of 5′-AGG-3′[25] and 5′-XAAA-3′, where X represented A, T, C or G.[26] The authors verified that the A, T, C and G bases could be directly identified by their ARP translocation time and residual current at femtomolar concentrations (Fig. 3a–d) without any modification, labelling and enzyme processing steps.[26] This study demonstrated the possibility that ARP systems could be utilized for highly sensitive and specific detection of single base variations, including the identification of gene mutations and base modifications. Later, Long's group[27] reported that an ARP system could discriminate methylcytosine (mC) from C (5′-CAAA-3′ vs. 5′-mCAAA-3′) in serum. The translocation frequency of methylated cytosine correlated with its relative concentration (Fig. 3e), suggesting that this approach could facilitate the quantification of such methylation-induced nanopore events. The ARP can discriminate the subtle difference between mC and C without any labeling or modification in both the conductance and dwell time (which increases the assay accuracy) with a zero-background signal in the presence of serum, which shows the possibility of clinical applications.

## 4. Direct detection of long oligonucleotides and oligonucleotides with the secondary structure in the ARP

The major challenge for nucleic acid detection using ARP is its extremely low capture efficiency for nucleic acid targets longer than 10 nucleotides. However, the Gu group[22] has identified a pH taxis-mimicking mechanism (Fig. 4a) where regulating the pH on one side of the pore can be used to capture targets from the opposite side of the pore, to control the capture of long RNA and DNA oligonucleotides with high sensitivity, even at +10 mV with a *trans* pH of 2.1–2.6 (Fig. 4b). For all *trans* pH values tested, the *cis* DNA capture rate ($k_{on}$) could be enhanced by increasing the voltage. For example, the $k_{on}$ for *trans* pH 3.4 increased approximately 13-fold from 0.21 ± 0.03 $\mu M^{-1}$ $s^{-1}$ to 2.8 ± 0.4 $\mu M^{-1}$ $s^{-1}$ as the voltage was increased from +20 mV to +80 mV (Fig. 4c, left). This capture efficiency (sensitivity) is superior to that of the alpha-hemolysin pore, which was approximately 1 $\mu M^{-1}$ $s^{-1}$ at +100 mV,[28] and almost zero at +80 mV. Furthermore, lowering the *trans* pH also increased

sensitivity. For example, the $k_{on}$ at 80 mV increased from 2.8 ± 0.4 $\mu M^{-1}$ $s^{-1}$ to 4.2 ± 0.5 $\mu M^{-1}$ $s^{-1}$ when the *trans* pH was decreased from pH 3.4 to pH 2.1 (Fig. 4c, left). At the same time, this hill-shaped $\tau$–*V* relationship (*trans* pH 3.4 and pH 3.2) suggested that the captured DNA could pass through the pore above the peak voltage (between +30 to +40 mV), but returns to the *cis* solution at lower voltages.[29] From *trans* pH 2.6 to 2.1, the monotonic $\tau$–V relationship suggested that the captured DNA could translocate through the pore at all voltages. The observed DNA translocation time ($\tau$) ranged between 0.83 and 40 ms for voltages between +10 mV and +80 mV at *trans* pH 3.4–2.1 (Fig. 4c, right). This time scale is longer than for DNA translocation through alpha-hemolysin (~100 μs), demonstrating the ability of ARP to temporally identify the DNAs with different lengths (Fig. 4d). The prolonged ARP translocation time was reported to be caused by the protonation of the N3 groups of adenine ($pK_a$ = 3.5) and cytosine ($pK_a$ = 4.2) when translocating the pore due to low pH inside the channel (pH 3.4–2.1). This protonation may also change DNA interactions with the pore lumen. These results demonstrated that methodology changes could increase sensitivity while decelerating the translocation of long oligonucleo-tides in the ARP, a highly desired property for any nanopore biosensing platform.

The voltage-dependence of $k_{on}$ may provide information about the nature of DNA capture and translocation through ARP. In a capture event, a DNA molecule first migrates from the bulk solution to the pore opening, which is a diffusive step that is biased by the electric field outside the pore entrance.[30–32]

This step is characterized by a linear $k_{on}$–V relationship.[30,31,33] Following this diffusion step, the DNA threads into the pore for translocation, which requires surmounting an energy barrier due to nanopore confinement of the DNA end and/or unfavorable DNA–pore interactions.[30,31,33] This step is characterized by $k_{on}$ exponentially changing with the applied voltage ($k_{on} \sim \exp(V)$).[30,31,33] DNA capture and translocation through ARP can be considered as a voltage-biased, diffusion-limited procedure, due to better linear fitting of the $k_{on}$–V curves as *trans* pH decreases (Fig. 5a, left). In order to understand the mechanisms of remote pH-activation of ARP for DNA capturing, the authors kept *cis* pH at 7.4 and observed the continuous increase of *cis* DNA capture rate at +40 mV by lowering the *trans* pH from 7.4 to 2.1 (Fig. 5a, right, solid circles). The results demonstrated four different DNA capture rates: (1) $k_{on}$ remained zero (trans pH 7.4–5.0); (2) $k_{on}$ moderately increased (trans pH 5.0–3.7); (3) $k_{on}$ increased >10-fold (trans pH 3.7 to 2.6); and (4) $k_{on}$ reached saturation (trans pH 2.3 to pH 2.1). This *trans* pH-dependent $k_{on}$ ($k_{on} = k_{on\_S}/(1 + 10^{\text{trans pH–pH50}})$) was consistent with the pH-dependent protona tion probability ($P_{RH} = 1/(1 + 10^{\text{pH–pKa}})$), where $P_{RH}$ (between 0 and 1) is the probability of a residue (R) in the protonated state ($RH^+$), and $pK_a$ is the pH value at which $P_{RH}$ = 50%. This correlation between *trans* pH-dependent $k_{on}$ and pH-dependent protonation probability strongly suggests that DNA capture is enhanced by pH-induced protonation of ARP, which was also confirmed by the current–voltage (*I*–*V*) curves of ARP at various *trans* pH values while the *cis* pH was held constant at pH 7.4. As the *trans* pH was lowered from 7.4 to 6.7, 5.1, 4.0, 3.7, and 3.2, $V_r$ trended to be more negative, from −29, to −26, −34, −38, −43, and −49 mV. The negative polarity of $V_r$ indicates that aerolysin is an anion ($Cl^-$)-selective pore. Lowering the *trans* pH can greatly enhance anion selectivity (Fig. 5b, left) and ARP offers

rich protonatable residues, such as E237, E252, E254 and E258 close to the *trans* entrance and D209 and D216 close to the *cis* entrance (Fig. 5b, right). This pH-dependent anion flow suggests that a protonation-induced electro-osmotic flow drives DNA capture by ARP. Net $Cl^-$ flow was maximized around pH 3.0 ($J/J_0$ = 95% at *trans* pH 3.2). Below pH 3.0, the electro-osmotic effect became saturated (Fig. 5a, right, empty circles), but $k_{on}$ continued to increase. This could be caused by low *trans* pH (pH 3.0 or lower) that may "remotely" protonate residues at the *cis* entrance (e.g. D209 and D216) through a $[H^+]$ gradient across the pore. To protonate the *cis* entrance D209 and D216 ($pK_a$ = 3.86), the *trans* pH must be lower than this $pK_a$ due to a pH gradient along the pore. This is consistent with the result that the $k_{on}$-trans pH curve gave $pH_{50}$ = 3.2, lower than $pK_a$ = 3.86.

The above discussed *cis* DNA capturing regulation by *trans* pH, especially the "remotely" protonate residues at the *cis* entrance through a $[H^+]$ gradient across the pore channel is a newly reported mechanism. This is a simple and easy-to-operate approach to noncovalently transform ARP into a highly nucleic acid-sensitive nanopore. Furthermore, the same mechanism is applicable to the widely used alpha-hemolysin pore, where lowering the pH at the *cis* side enhances DNA capture on the *trans* side, *vice versa* (Fig. 5c). This mechanism could be confirmed by ARP mutagenesis studies by observing that E254R and E252R (at *trans* opening) mutagenesis can increase $k_{on}$ (DNA in *cis*) while both *cis* and *trans* pH remained at pH 7.4. Studies have shown that placing charged motifs at the protein pore entrances can enhance the DNA capture efficiency.[34] Based on structural information and the highly charged walls of the ARP pore,[12] Dr Long's group has recently studied the effects of site-directed muta-genesis in ARP on DNA capturing.[35] To investigate the selectivity and sensitivity of ARP, the authors generated R220E and K238E ARP mutants, and compared their DNA–pore interactions with wild-type (WT) ARP (Fig. 1c). Dr Long's group also studied DNAs with secondary structures and their ARP capture, finding that a structured oligonucleotide (G-quadruplex) is effectively unfolded into a linear form by replacing the cation $K^+$ with $Mg^{2+}$, and that this linear DNA undergoes translocation through the ARP (Fig. 5d). The results demonstrated a proportional relationship between the length of oligonucleotides and the duration time with a trans-location velocity as low as 0.70–0.13 ms $nt^{-1}$ at +140 mV, which is hundreds of times slower than that detected with the alpha-hemolysin nanopore.

Molecular dynamics simulations play an important role in exploring nanopore properties and DNA–pore interaction.[36–38] Molecular dynamics simulations could provide useful information on the mechanisms and principles of the observed "remote activation of ARP by the pH taxis-mimicking mechanism". Molecular dynamics simulations can show the electrical field distribution, magnitude and direction around ARP openings; determine the effective force on the target; dielectrophoresis flow as a function of the applied voltage; the process of DNA target capturing in the pore and so on.[39] This method, experimental results combined with the computing approach, can be applied to the ARP in the future studies.

## 5. Perspectives: possible applications of ARP in sequencing and biomarker sensing

Nanopores have been developed for next-generation sequencing methods for decades that use DNA polymerase to control DNA threading through the pore in a controlled single base manner.[40–42] The commercially available MinIon (Oxford Nanopore Technologies) is a portable instrument that contains hundreds of alpha-hemolysin nanopores embedded within a synthetic membrane[43] and has been used to test clinical samples.[44,45] The MspA nanopore is a newly developed nano-pore system for sequencing.[46] But all of them still face two challenges: fast translocation of a single base and distinguish global nucleotide repeats using the residual current,[46–49] which greatly increases the error rate. In ARP, it is possible to present the target DNA and polymerase in the *cis* chamber while using a low pH in the *trans* chamber, with the advantages of slow DNA translocation of DNA in ARP, as we discussed above, it is very promising to achieve higher sensitivity and specificity (accuracy) in ARP for sequencing.

There is a growing trend for the development of bio-sensors[50] for genetic and epigenetic detection, cancer- and disease-related biomarker detection and identification, which can analyze clinical or patient's samples,[28,51] and substantial effort is being put in to create portable and robust protein nanopore devices.[52–55] However, all nanopore sensors are facing two common challenges: low detection efficiency and fast translocation speed.[56] These problems are particularly important in clinical studies, where there are usually extremely low physiological concentrations of biomarkers in complex biological samples.

Decelerated translocation of nucleic acids through the nanopore is a desirable property for sequencing and high performance detection.[56] Enhancing the capture of a target while slowing down its translocation appears contradictory, but this can be easily controlled by adjusting pH in ARP as we discussed above. A transmembrane salt gradient has also been proven to be an effective way to enhance DNA capture and reduce the translocation speed in both protein and synthetic nanopores.[28,31] More efforts are still urgently needed in this direction for developing versatile and accurate nanopore sensors and sequencing platforms. We can envision that ARP can be a promising tool for analyzing oligonucleotides, single-nucleotide alterations (*e.g.*, driver mutations), epigenetic modifications, DNA damage, microRNAs and circulating DNAs in a reliable manner, as ARP has the advantages of high sensitivity and specificity towards these targets and it is highly promising in these applications.

## Acknowledgements

This study was supported by the National Institutes of Health grants GM114204 (Li-Qun Gu) and HG009338 (Kent Gates and Li-Qun Gu). We thank Dr Christopher Lyon for the helpful discussions and revisions on this manuscript.

## References

1. Howard SP and Buckley JT, J. Bacteriol, 1985, 163, 336–340. [PubMed: 3891735]
2. Howard SP, Garland WJ, Green MJ and Buckley JT, J. Bacteriol, 1987, 169, 2869–2871. [PubMed: 3584074]

3. Stefureac R, Long Y.-t., Kraatz H-B, Howard P and Lee JS, Biochemistry, 2006, 45, 9172–9179. [PubMed: 16866363]
4. Stefureac R, Waldner L, Howard P and Lee JS, Small, 2008, 4, 59–63. [PubMed: 18058890]
5. Pastoriza-Gallego M, Rabah L, Gibrat G, Thiebot B, van der Goot FG, Auvray L, Betton JM and Pelta J, J. Am. Chem. Soc, 2011, 133, 2923–2931. [PubMed: 21319816]
6. Merstorf C. l., Cressiot B, Pastoriza-Gallego M, Oukhaled A, Betton J-M, Auvray L and Pelta J, ACS Chem. Biol, 2012, 7, 652–658. [PubMed: 22260417]
7. Fennouri A, Przybylski C, Pastoriza-Gallego M, Bacri L, Auvray L and Daniel R, ACS Nano, 2012, 6, 9672–9678. [PubMed: 23046010]
8. Fennouri A, Daniel R. g., Pastoriza-Gallego M, Auvray L, Pelta J and Bacri L, Anal. Chem, 2013, 85, 8488–8492. [PubMed: 23992452]
9. Wang Y, Montana V, Grubišić V, Stout RF, Jr., Parpura V and Gu L-Q, ACS Appl. Mater. Interfaces, 2014, 7, 184–192. [PubMed: 25511125]
10. Pastoriza-Gallego M, Breton MF, Discala F, Auvray L, Betton JM and Pelta J, ACS Nano, 2014, 8, 11350–11360. [PubMed: 25380310]
11. Cao C, Ying Y-L, Gu Z and Long Y-T, Anal. Chem, 2014, 86, 11946–11950. [PubMed: 25457124]
12. Baaken G, Halimeh I, Bacri L, Pelta J, Oukhaled A and Behrends JC, ACS Nano, 2015, 9, 6443–6449. [PubMed: 26028280]
13. Cressiot B, Braselmann E, Oukhaled A, Elcock AH, Pelta J and Clark PL, ACS Nano, 2015, 9, 9050–9061. [PubMed: 26302243]
14. Hu Z-L, Li Z-Y, Ying Y-L, Zhang J, Cao C, Long Y-T and Tian H, Anal. Chem, 2018, 90, 4268–4272. [PubMed: 29516718]
15. Xi D, Li Z, Liu L, Ai S and Zhang S, Anal. Chem, 2018, 90, 1029–1034. [PubMed: 29210271]
16. Piguet F, Ouldali H, Pastoriza-Gallego M, Manivet P, Pelta J and Oukhaled A, Nat. Commun, 2018, 9, 966. [PubMed: 29511176]
17. Li S, Cao C, Yang J and Long Y-T, ChemElectroChem, 2018, 5, 1–5.
18. Payet L, Martinho M, Merstorf C, Pastoriza-Gallego M, Pelta J, Viasnoff V, Auvray L, Muthukumar M and Mathe J, Biophys. J, 2015, 109, 1600–1607. [PubMed: 26488651]
19. Iacovache I, De Carlo S, Cirauqui N, Dal Peraro M, Van Der Goot FG and Zuber B, Nat. Commun, 2016, 7, 12062. [PubMed: 27405240]
20. Degiacomi MT, Iacovache I, Pernot L, Chami M, Kudryashev M, Stahlberg H, Van Der Goot FG and Dal Peraro M, Nat. Chem. Biol, 2013, 9, 623. [PubMed: 23912165]
21. Cao C, Ying YL, Hu ZL, Liao DF, Tian H and Long YT, Nat. Nanotechnol, 2016, 11, 713–718. [PubMed: 27111839]
22. Wang Y, Tian K, Du X, Shi R and Gu L-Q, Anal. Chem, 2017, 89(24), 13039–13043. [PubMed: 29183111]
23. Cao C, Liao D-F, Yu J, Tian H and Long Y-T, Nat. Protoc, 2017, 12, 1901–1911. [PubMed: 28837133]
24. Cao C, Yu J, Wang Y-Q, Ying Y-L and Long Y-T, Anal. Chem, 2016, 88, 5046–5049. [PubMed: 27120503]
25. Cao Chan LD, Yilun Y and Yitao L, Acta Chim. Sin, 2016, 74, 734–737.
26. Cao C, Yu J, Li MY, Wang YQ, Tian H and Long YT, Small, 2017, 13, 1702011.
27. Yu J, Cao C and Long Y-T, Anal. Chem, 2017, 89(21), 11685–11689. [PubMed: 28988479]
28. Wang Y, Zheng D, Tan Q, Wang MX and Gu LQ, Nat. Nanotechnol, 2011, 6, 668–674. [PubMed: 21892163]
29. Tian K, He Z, Wang Y, Chen SJ and Gu LQ, ACS Nano, 2013, 7, 3962–3969. [PubMed: 23550815]
30. Muthukumar M, J. Chem. Phys, 2010, 132, 195101. [PubMed: 20499989]
31. Wanunu M, Morrison W, Rabin Y, Grosberg AY and Meller A, Nat. Nanotechnol, 2010, 5, 160–165. [PubMed: 20023645]
32. Rowghanian P and Grosberg AY, Phys. Rev. E: Stat. Phys., Plasmas, Fluids, Relat. Interdiscip. Top, 2013, 87, 042722.

33. Wang Y, Tian K, Lehr H, Ritzo B and Gu L-Q, Nanoscale, 2014, 6, 11372–11379. [PubMed: 25144935]
34. Maglia G, Restrepo MR, Mikhailova E and Bayley H, Proc. Natl. Acad. Sci. U. S. A, 2008, 105, 19720–19725. [PubMed: 19060213]
35. Wang Y-Q, Cao C, Ying Y-L, Li S, Wang M-B, Huang J and Long Y-T, ACS Sens, 2018, 3(4), 779–783. [PubMed: 29619834]
36. Aksimentiev A and Schulten K, Biophys. J, 2005, 88, 3745–3761. [PubMed: 15764651]
37. Bhattacharya S, Derrington IM, Pavlenok M, Niederweis M, Gundlach JH and Aksimentiev A, ACS Nano, 2012, 6, 6960–6968. [PubMed: 22747101]
38. Bhattacharya S, Muzard J, Payet L, Mathé J, Bockelmann U, Aksimentiev A and Viasnoff V, J. Phys. Chem. C, 2011, 115, 4255–4264.
39. Tian K, Decker K, Aksimentiev A and Gu L-Q, ACS Nano, 2017, 11, 1204–1213. [PubMed: 28036167]
40. Laszlo AH, Derrington IM, Ross BC, Brinkerhoff H, Adey A, Nova IC, Craig JM, Langford KW, Samson JM and Daza R, Nat. Biotechnol, 2014, 32, 829–833. [PubMed: 24964173]
41. Manrao EA, Derrington IM, Laszlo AH, Langford KW, Hopper MK, Gillgren N, Pavlenok M, Niederweis M and Gundlach JH, Nat. Biotechnol, 2012, 30, 349–353. [PubMed: 22446694]
42. Cherf GM, Lieberman KR, Rashid H, Lam CE, Karplus K and Akeson M, Nat. Biotechnol, 2012, 30, 344–348. [PubMed: 22334048]
43. Eisenstein M, Nat. Biotechnol, 2012, 30, 295–296. [PubMed: 22491260]
44. Votintseva AA, Bradley P, Pankhurst L, del Ojo Elias C, Loose M, Nilgiriwala K, Chatterjee A, Smith EG, Sanderson N and Walker TM, J. Clin. Microbiol, 2017, 55, 1285–1298. [PubMed: 28275074]
45. Greninger AL, Schneider BS, Chiu CY, Stryke D, Yu G, Muyembe-Tamfum J-J, Linnen JM, Bouquet J, Mbala P and Mulembakani P, Genome Med, 2015, 7, 99. [PubMed: 26416663]
46. Derrington IM, Butler TZ, Collins MD, Manrao E, Pavlenok M, Niederweis M and Gundlach JH, Proc. Natl. Acad. Sci. U. S. A, 2010, 107, 16060–16065. [PubMed: 20798343]
47. Koren S and Phillippy AM, Curr. Opin. Microbiol, 2015, 23, 110–120. [PubMed: 25461581]
48. De Bustos A, Cuadrado A and Jouve N, Sci. Rep, 2016, 6, 36665. [PubMed: 27819354]
49. Feng Y, Zhang Y, Ying C, Wang D and Du C, Genomics, Proteomics Bioinf, 2015, 13, 4–16.
50. Gu L-Q, Ritzo B and Wang Y, Nat. Nanotechnol, 2012, 7, 212. [PubMed: 22481488]
51. Wang Y, Tian K, Shi R, Gu A, Pennella M, Alberts L, Gates KS, Li G, Fan H and Wang MX, ACS Sens, 2017, 2, 975–981. [PubMed: 28750524]
52. Cockroft SL, Chu J, Amorin M and Ghadiri MR, J. Am. Chem. Soc, 2008, 130, 818–820. [PubMed: 18166054]
53. Kawano R, Osaki T, Sasaki H and Takeuchi S, Small, 2010, 6, 2100–2104. [PubMed: 20839243]
54. Shim JW and Gu LQ, Anal. Chem, 2007, 79, 2207–2213. [PubMed: 17288404]
55. Kang XF, Cheley S, Rice-Ficht AC and Bayley H, J. Am. Chem. Soc, 2007, 129, 4701–4705. [PubMed: 17375923]
56. Squires A and Meller A, Biophys. J, 2013, 105, 543–544. [PubMed: 23931300]

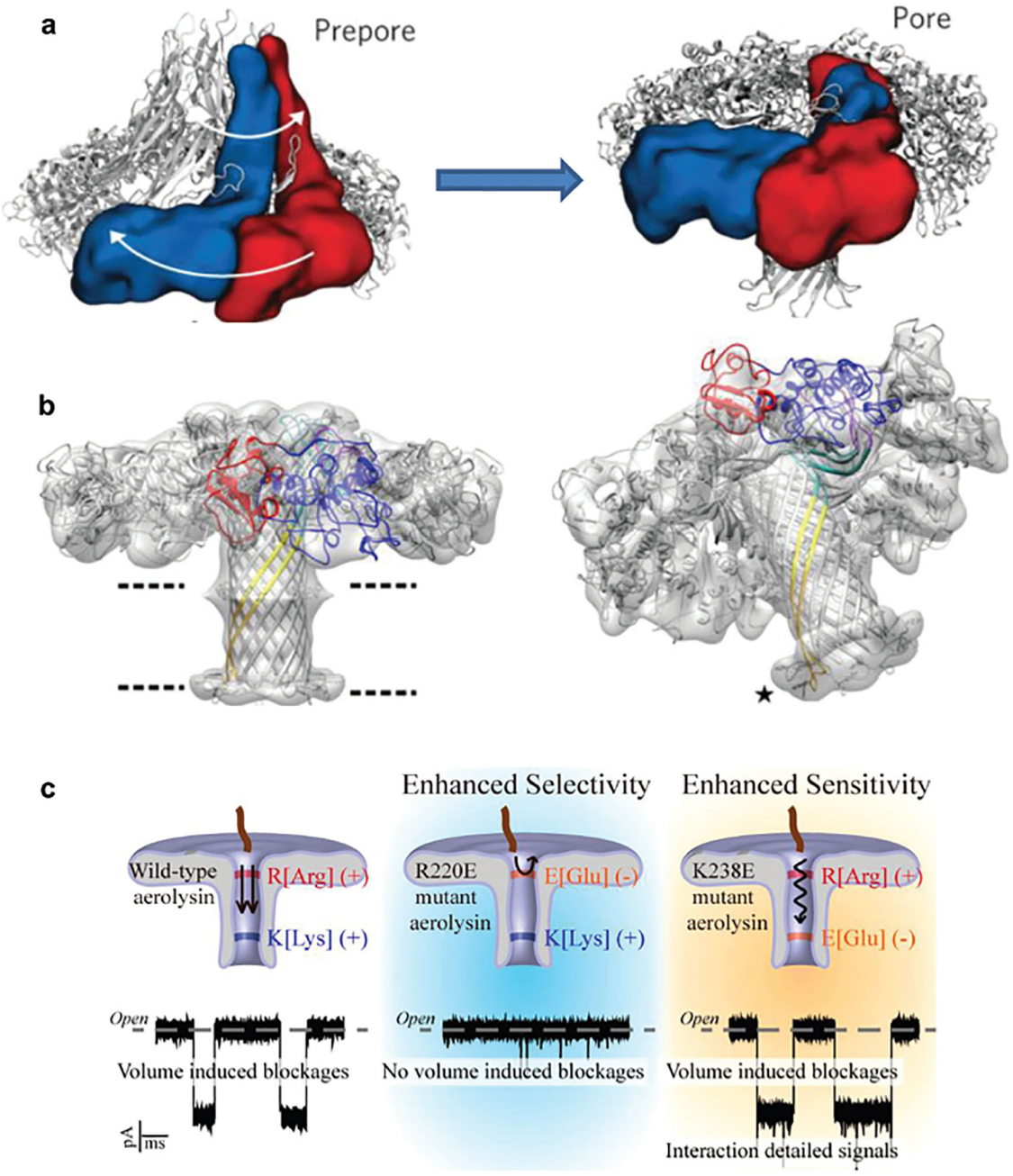


**Fig. 1.**

(a) Ribbon and space-filling (for two representative monomers) representation of the pre-pore and the membrane-inserted state, illustrating the overall swirling movement and involving a collapse of the structure. Reprinted with permission from DOI: 10.1038/nchembio.1312, Nat. Chem. Biol., 2013. (b) The aerolysin pore structure obtained from the quasipore map (left); tilted view showing the fit of the loops at the end of the trans-membrane β-barrel (asterisk), upon crossing the bilayer the tips of the β-barrel loops fold back forming a rivet (right). Reprinted with permission from DOI: 10.1038/ncomms12062, *Nat.* Commun., 2016. (c) Site-directed mutagenesis regulates the selectivity and sensitivity

of the aerolysin pore. Reprinted with permission from DOI: 10.1021/acssensors.8b00021, *ACS Sens.*, 2018.

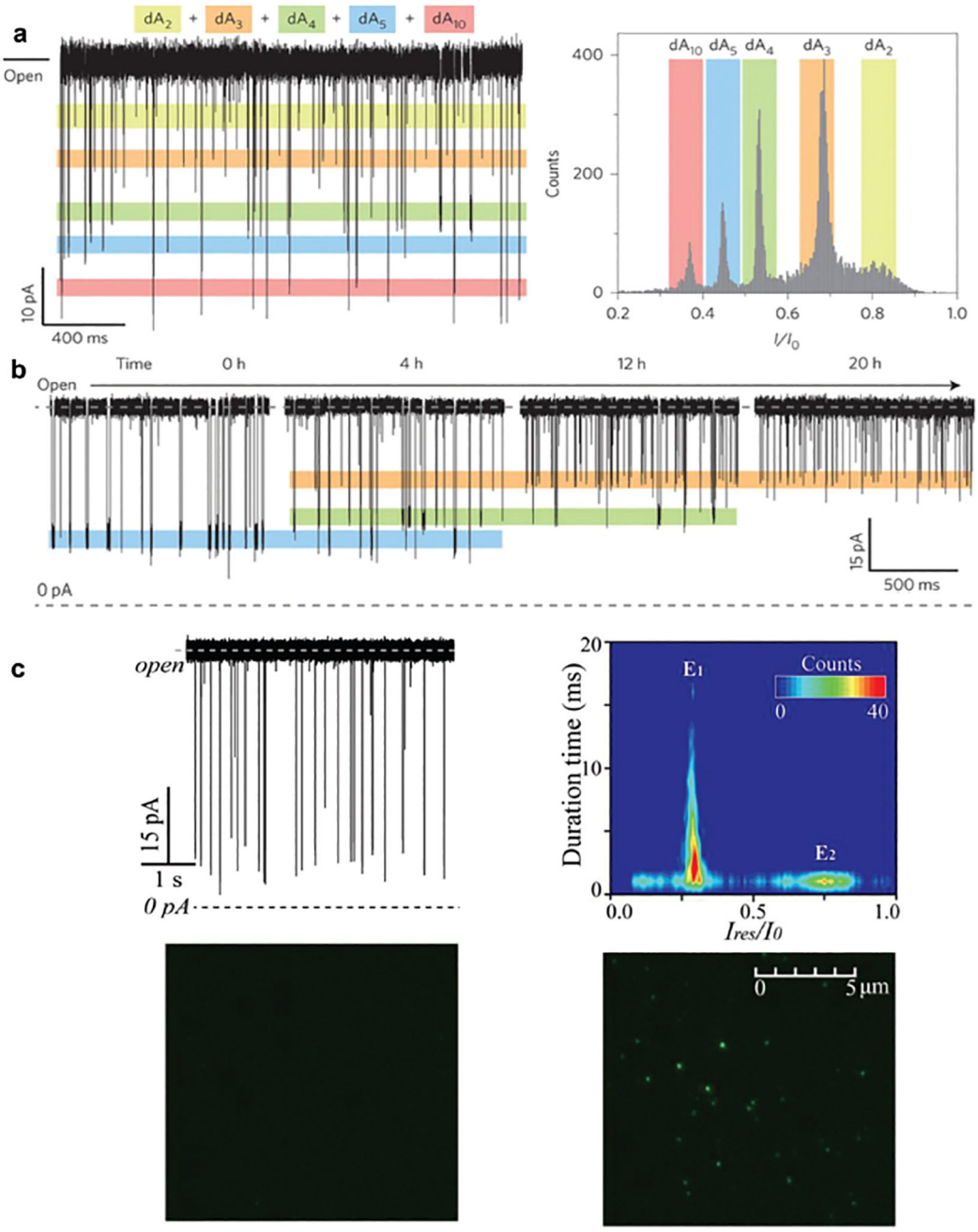


**Fig. 2.**

(a) A continuous trace showing the distinctive current levels for $dA_n$ (left) and their histograms in a mixture of $dA_n$ ($n$ = 2, 3, 4, 5 and 10). (b) In the presence of 1.0 μM $dA_5$ and 2000 U ExoI, demonstrating the cleavage process of $dA_5$into short fragments at 0, 4, 12 and 20 h. Reprinted with permission from DOI: 10.1038/NNAN0.2016.66, *Nat. Nano.*, 2016. (c) Raw current traces produced by DNA 5'-ACTG-3' (with a 5'-hexachloro-fluorescein tag) and its contour plots produced by DNA (upper panel). The TIRF images of solution collected from the *trans* side of aerolysin in the absence (left) and presence of DNA (right)

after continuous single-channel recording for 6 h (bottom panel). Reprinted with permission from DOI: 10.1021/acs.analchem.6b01514, *Anal. Chem.*, 2016.

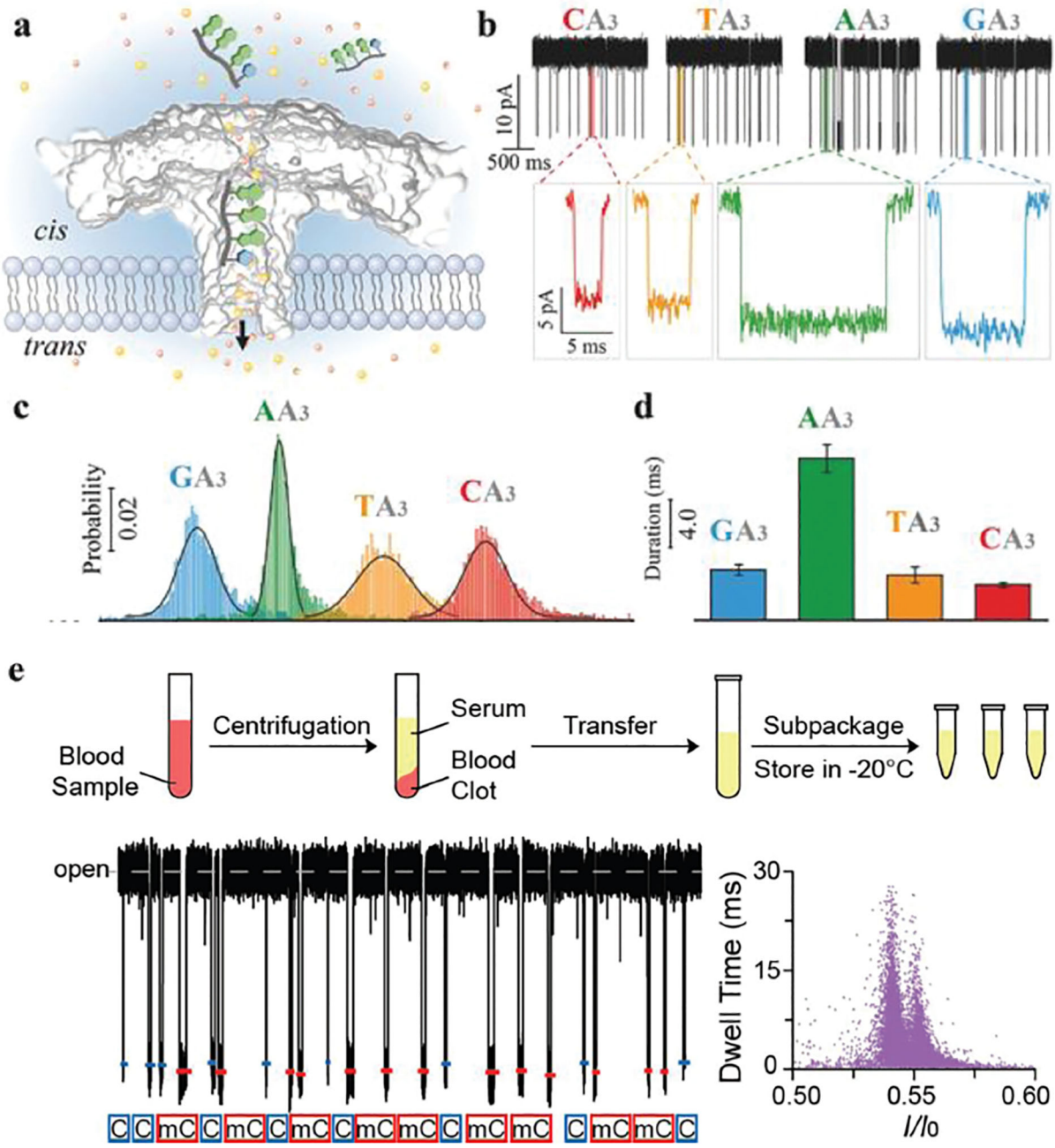


**Fig. 3.**

(a) Aerolysin inserted into the lipid bilayer from the *cis* chamber. The ssDNA oligomers were added into the *cis* solution after applying a positive potential from the *trans* side. With the *cis* solution grounded, the negatively charged ssDNA was able to traverse the aerolysin from the *cis* to the *trans* chamber and induce a blockade current signal. (b) Single-channel recording of $CA_3$ (red), $TA_3$ (orange), $AA_3$ (green), and $GA_3$ (blue), and the corresponding typical current traces. (c) The residual current histograms (top) and scatter plots (bottom) of the duration versus residual current of $CA_3$, $TA_3$, $AA_3$, and $GA_3$, respectively. All residual current histograms were fitted to Gaussian distributions. (d) Durations recorded for the

additions of $CA_3$, $TA_3$, $AA_3$, and $GA_3$ into the aerolysin nanopore, respectively. Reprinted with permission from DOI: 10.1002/smll.201702011, *Small*, 2017. (e) Detection of methylated and unmethylated DNA in serum. Upper panel: Preparation of serum samples. Human serum was centrifuged, apportioned, and stored at −20 °C before usage. Lower panel: Assignments of C-DNA (blue) and mC-DNA (red) in raw current traces. Two colored short lines and marks were assigned to C-DNA and mC-DNA, respectively. Reprinted with permission from DOI: 10.1021/acs.analchem.7b03133, *Anal. Chem.*, 2017.

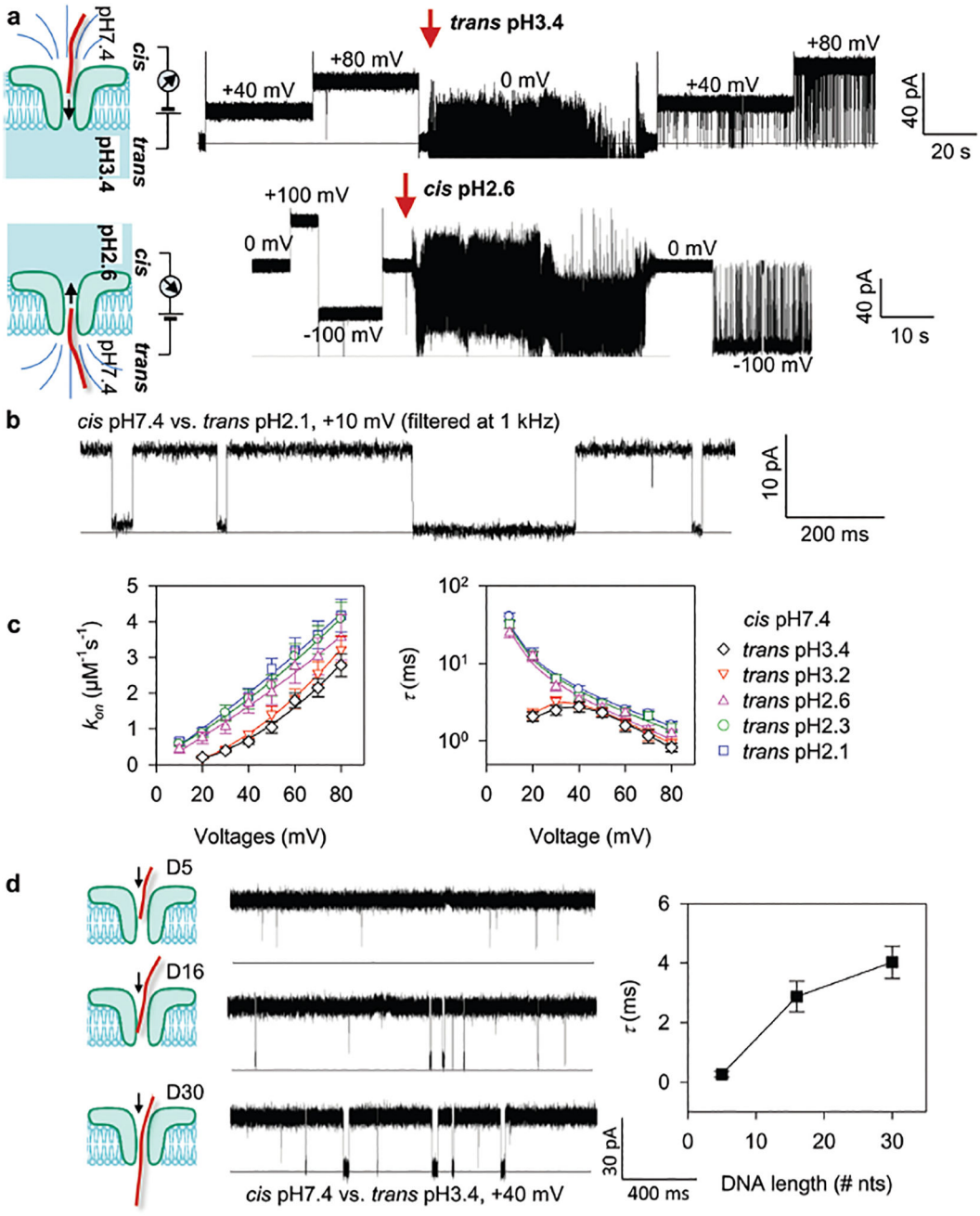


**Fig. 4.**

(a) Trapping of a 16 nt DNA from *cis* (up panel) or *trans* (bottom) while lowering the pH at the *trans* or *cis* side in the aerolysin pore. (b) The representative single channel current trace showing that the activated aerolysin pore can capture a 16 nt DNA with high sensitivity even at 10 mV with a prolonged translocation time. (c) Voltage-dependence of the DNA capture rate ($k_{on}$) (left) and block duration ($\tau$, right) at various acidic *trans* pH. (d) Discriminating DNA of different lengths (5-, 16- and 30 nt) from their block durations. Reprinted with permission from DOI: 10.1021/acs.analchem.7b03979, *Anal. Chem.*, 2017.

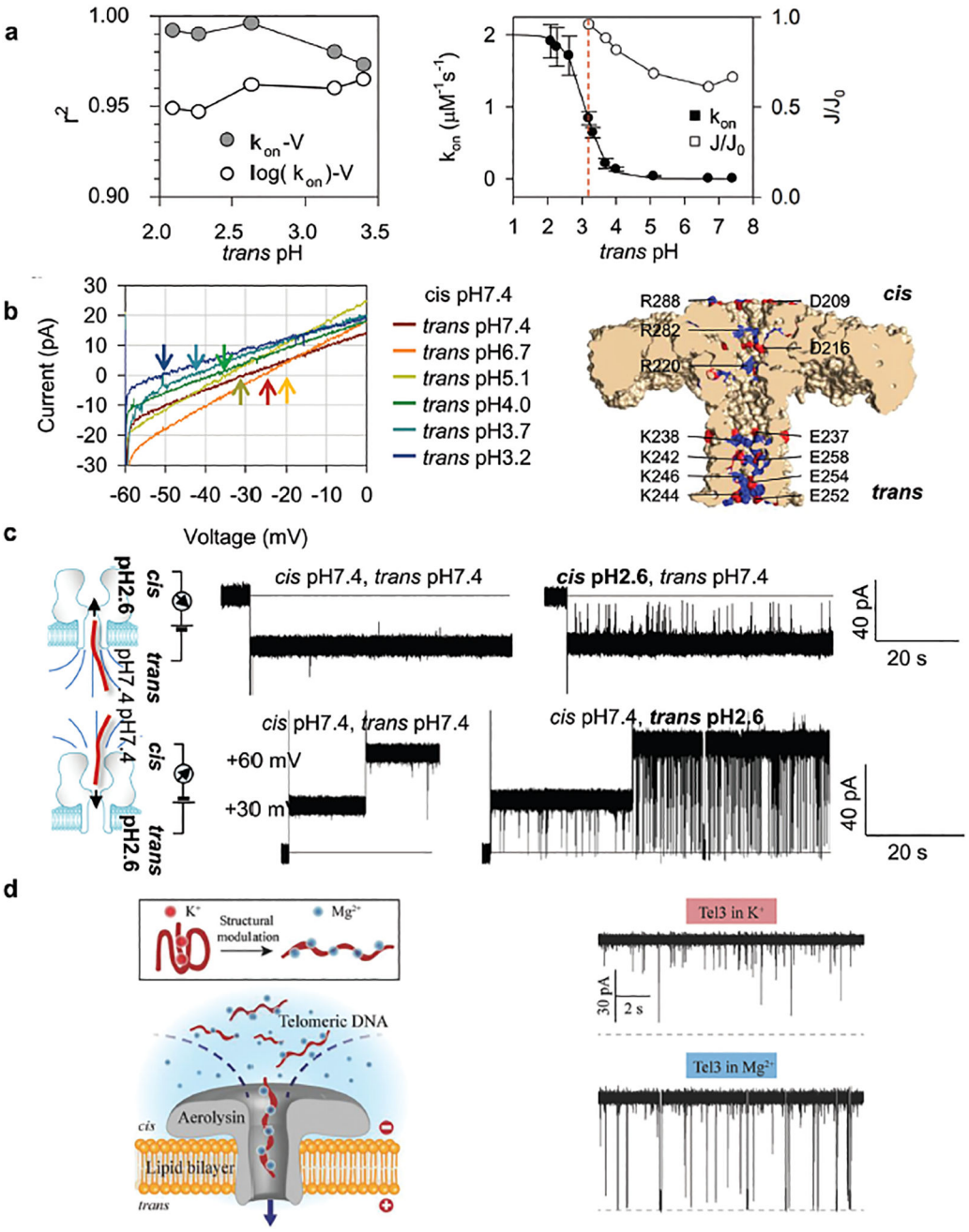


**Fig. 5.**

(a) Comparison of regression coefficients ($r^2$) for linear regression fitting of $k_{on}$–$V$ curves on the linear $k_{on}$ scale and on the log $k_{on}$ scale (left); the *trans* pH-dependent relative net anion flow $J/J_0$ and the $k_{on}$-trans pH curve (right). (b) Current–voltage ($I$–$V$) curves of aerolysin at various *trans* pH. Arrows in different colors mark the reverse potential ($V_r$) (left); a cartoon showing charge distribution at the *cis* and trans entrance (right). (c) Trapping of a 16 nt DNA from *trans* (up panel) or *cis* (bottom) while lowering the pH at the *trans* or *cis* side in the alpha-hemolysin pore. Reprinted with permission from DOI: 10.1021/acs.analchem.7b03979, *Anal. Chem.*, 2017. (d) A cartoon showing a G-quadruplex structure unfolding

into a linear format (left) and its capturing (10 μM) in the aerolysin pore (right, $K^+$ (upper) or $Mg^{2+}$ (bottom)). Reprinted with permission from DOI: 10.1002/smll.201704520, *Small*, 2018.